

Chapter 2

Electronic and Transport Properties of Graphene

2.1 Introduction

Graphene has received a great attention since it was first isolated by Nobel Laureates Konstantin Novoselov and Andre K. Geim in 2004. The reason for such excitement is that graphene is the first truly 2D crystal ever observed in nature and possesses remarkable electrical, chemical and mechanical properties. Furthermore, electrons in graphene show a quasi-relativistic behavior, and the system is therefore an ideal candidate for the test of quantum field-theoretical models that have been developed in high-energy physics. Most prominently, electrons in graphene may be viewed as massless charged fermions existing in 2D space, particles that one usually does not encounter in our three-dimensional world. Indeed, all massless elementary particles, such as photons or neutrinos, happen to be electrically neutral. Graphene is therefore an exciting bridge between condensed matter and high-energy physics, and the research on its electronic properties unites scientists with various thematic backgrounds.

Graphene is also an attractive material for spintronics due to the theoretical possibility of long spin lifetimes arising from low intrinsic SOC and weak hyperfine interaction [1]. However, Hanle spin precession measurements and non-local spin valve geometry have reported spin lifetimes that are orders of magnitude shorter than expected theoretically [2–5]. Several studies have investigated spin relaxation including the roles of impurity scattering [5] and graphene thickness [6] and specially, ferromagnet contact-induced spin relaxation was predicted to be responsible for the short spin lifetimes observed in experiments [7]. However, these explanations have not given a satisfying answer for the discrepancy between theoretical results and experimental data. This has prompted theoretical studies of the extrinsic sources of spin relaxation such as impurity scattering [8], ripples [1], and substrate effects [9]. The problem remains however still puzzling and unsolved.

In this chapter, we will briefly review some theoretical and experimental results about fundamental electric and spin transport properties of graphene. Firstly, we will derive graphene band structure and massless Dirac equation for graphene in

Sect. 2.2. Next, some experimental and theoretical studies about transport properties of graphene are discussed in Sect. 2.3. Section 2.4 discusses some aspects of SOC in graphene, which plays an important role for studying spin relaxation in Chap. 5.

2.2 Graphene and Dirac Fermions

The most interesting property of graphene might be the Dirac-cone energy dispersion. This is the consequence of sp^2 hybridization and graphene symmetry. In this section, I briefly review its structure, the commonly used tight-binding (TB) description and the deviation of the linear energy dispersion of graphene.

2.2.1 Graphene

Graphene is a single atomic layer of graphite, an allotrope of carbon that is made up of very tightly bonded carbon atoms organised into a hexagonal lattice. What makes graphene so special is its sp^2 hybridization and very thin atomic thickness (see Fig. 2.1). These properties are what enable graphene to break so many records in terms of strength, electricity, heat conduction, etc.

Carbon is a common element in the nature, with atomic number 6, group 14 on the periodic table. The electronic configuration of carbon is $1s^2 2s^2 2p^2$ which shows that carbon has 4 electrons ($2s$ and $2p$) in its outer shell which is available for forming chemical bonds. In graphene, these four valence electrons form sp^2 hybridization in which three electrons are distributed into three in-plane σ bonds, which are strongly covalent, determining the energetic stability and the elastic properties of graphene.

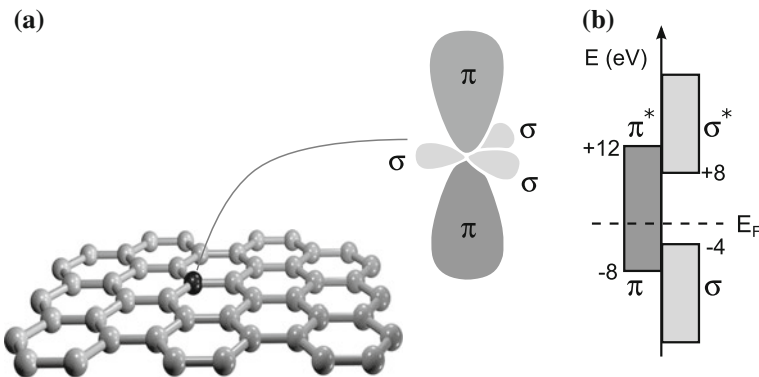


Fig. 2.1 Electronic structure of graphene **a** Graphene sample and the sp^2 hybridization in graphene. **b** Energy range of orbitals in graphene (Figure is taken from [10])

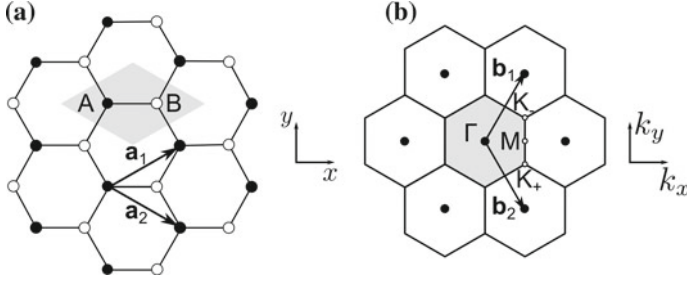


Fig. 2.2 Real (a) and reciprocal (b) space of graphene lattice (Figure is taken from [10])

The remaining electron in the p_z orbitals, which is perpendicular to graphene plane, forms the π bond in graphene (See Fig. 2.1).

The calculation for the energy ranges of σ and π bands (See Fig. 2.1b) shows that only electrons in the π bond contribute to the electronic properties of graphene because the σ bands are far away from the Fermi level. Because of this, it is sufficient to treat graphene as a collection of atoms with single p_z orbitals per site.

In graphene, carbon atoms are located at the vertices of a hexagonal lattice. Graphene is a bipartite lattice which consists of two sublattices A and B and basis vectors ($\mathbf{a}_1, \mathbf{a}_2$) (See Fig. 2.2):

$$\mathbf{a}_1 = a \left(\frac{\sqrt{3}}{2}, \frac{1}{2} \right), \mathbf{a}_2 = a \left(\frac{\sqrt{3}}{2}, -\frac{1}{2} \right), \quad (2.1)$$

with $a = \sqrt{3}a_{cc}$, where $a_{cc} = 1.42 \text{ \AA}$ is the carbon-carbon distance in graphene. These basis vectors build a hexagonal Brillouin zone with two inequivalent points K and K' (K_+ and K_- respectively in Fig. 2.2) at the corners

$$\mathbf{K} = \frac{4\pi}{3a} \left(\frac{\sqrt{3}}{2}, -\frac{1}{2} \right), \mathbf{K}' = \frac{4\pi}{3a} \left(\frac{\sqrt{3}}{2}, \frac{1}{2} \right), \quad (2.2)$$

As mentioned above and from Bloch's theorem, we can write the wave function in the form of p_z orbitals wave function at sublattices A ($\varphi(\mathbf{r} - \mathbf{r}_A)$) and B ($\varphi(\mathbf{r} - \mathbf{r}_B)$)

$$\Psi(\mathbf{k}, \mathbf{r}) = c_A(\mathbf{k})\phi^A(\mathbf{k}, \mathbf{r}) + c_B(\mathbf{k})\phi^B(\mathbf{k}, \mathbf{r}) \quad (2.3)$$

where

$$\phi^A(\mathbf{k}, \mathbf{r}) = \frac{1}{\sqrt{N}} \sum_{\mathbf{R}_j} e^{i\mathbf{k} \cdot \mathbf{R}_j} \varphi(\mathbf{r} - \mathbf{r}_A - \mathbf{R}_j), \quad (2.4)$$

$$\phi^B(\mathbf{k}, \mathbf{r}) = \frac{1}{\sqrt{N}} \sum_{\mathbf{R}_j} e^{i\mathbf{k} \cdot \mathbf{R}_j} \varphi(\mathbf{r} - \mathbf{r}_B - \mathbf{R}_j), \quad (2.5)$$

where \mathbf{k} is the electron wavevector, N the number of unit cells in the graphene sheet, and \mathbf{R}_j is a Bravais lattice point.

Using the Schrödinger equation, $\mathcal{H}\Psi(\mathbf{k}, \mathbf{r}) = E\Psi(\mathbf{k}, \mathbf{r})$, one obtains a 2×2 eigenvalue problem,

$$\mathcal{H}(\mathbf{k}) \begin{pmatrix} c_A(\mathbf{k}) \\ c_B(\mathbf{k}) \end{pmatrix} = \begin{pmatrix} \mathcal{H}_{AA}(\mathbf{k}) & \mathcal{H}_{AB}(\mathbf{k}) \\ \mathcal{H}_{BA}(\mathbf{k}) & \mathcal{H}_{BB}(\mathbf{k}) \end{pmatrix} \begin{pmatrix} c_A(\mathbf{k}) \\ c_B(\mathbf{k}) \end{pmatrix} = E(\mathbf{k}) \begin{pmatrix} S_{AA}(\mathbf{k}) & S_{AB}(\mathbf{k}) \\ S_{BA}(\mathbf{k}) & S_{BB}(\mathbf{k}) \end{pmatrix} \begin{pmatrix} c_A(\mathbf{k}) \\ c_B(\mathbf{k}) \end{pmatrix}. \quad (2.6)$$

where $S_{\alpha\beta}(\mathbf{k}) = \langle \phi^\alpha(\mathbf{k}) | \phi^\beta(\mathbf{k}) \rangle$ and the matrix elements of the Hamiltonian are given by:

$$\mathcal{H}_{AA}(\mathbf{k}) = \frac{1}{N} \sum_{\mathbf{R}_i, \mathbf{R}_j} e^{i\mathbf{k} \cdot (\mathbf{R}_j - \mathbf{R}_i)} \langle \varphi^{A, \mathbf{R}_i} | \mathcal{H} | \varphi^{A, \mathbf{R}_j} \rangle \quad (2.7)$$

$$\mathcal{H}_{AB}(\mathbf{k}) = \frac{1}{N} \sum_{\mathbf{R}_i, \mathbf{R}_j} e^{i\mathbf{k} \cdot (\mathbf{R}_j - \mathbf{R}_i)} \langle \varphi^{A, \mathbf{R}_i} | \mathcal{H} | \varphi^{B, \mathbf{R}_j} \rangle, \quad (2.8)$$

with $\mathcal{H}_{AA} = \mathcal{H}_{BB}$ and $\mathcal{H}_{AB} = \mathcal{H}_{BA}^*$, and introducing the notation: $\varphi^{A, \mathbf{R}_i} = \varphi(\mathbf{r} - \mathbf{r}_A - \mathbf{R}_i)$ and $\varphi^{B, \mathbf{R}_i} = \varphi(\mathbf{r} - \mathbf{r}_B - \mathbf{R}_i)$.

If we neglect the overlap $s = \langle \varphi^A | \varphi^B \rangle$ between neighboring p_z orbitals, then, $S_{\alpha\beta}(\mathbf{k}) = \delta_{\alpha,\beta}$ and Eq. (2.6) becomes

$$\begin{pmatrix} \mathcal{H}_{AA}(\mathbf{k}) & \mathcal{H}_{AB}(\mathbf{k}) \\ \mathcal{H}_{BA}(\mathbf{k}) & \mathcal{H}_{BB}(\mathbf{k}) \end{pmatrix} \begin{pmatrix} c_A(\mathbf{k}) \\ c_B(\mathbf{k}) \end{pmatrix} = E(\mathbf{k}) \begin{pmatrix} c_A(\mathbf{k}) \\ c_B(\mathbf{k}) \end{pmatrix}. \quad (2.9)$$

If we consider only the first-nearest-neighbors interactions then

$$\begin{aligned} \mathcal{H}_{AB}(\mathbf{k}) &= \langle \varphi^{A,0} | \mathcal{H} | \varphi^{B,0} \rangle + e^{-i\mathbf{k} \cdot \mathbf{a}_1} \langle \varphi^{A,0} | \mathcal{H} | \varphi^{B,-\mathbf{a}_1} \rangle + e^{-i\mathbf{k} \cdot \mathbf{a}_2} \langle \varphi^{A,0} | \mathcal{H} | \varphi^{B,-\mathbf{a}_2} \rangle \\ &= -\gamma_0 \alpha(\mathbf{k}) \end{aligned} \quad (2.10)$$

where γ_0 stands for the transfer integral between first neighbors π orbitals ($\gamma_0 = 2.7\text{eV}$ in this thesis) and $\alpha(\mathbf{k})$ is given by:

$$\alpha(\mathbf{k}) = (1 + e^{-i\mathbf{k} \cdot \mathbf{a}_1} + e^{-i\mathbf{k} \cdot \mathbf{a}_2}). \quad (2.11)$$

Taking $\mathcal{H}_{AA}(\mathbf{k}) = \mathcal{H}_{BB}(\mathbf{k}) = 0$ as the energy reference, we can write $\mathcal{H}(\mathbf{k})$ as:

$$\mathcal{H}(\mathbf{k}) = \begin{pmatrix} 0 & -\gamma_0 \alpha(\mathbf{k}) \\ -\gamma_0 \alpha(\mathbf{k})^* & 0 \end{pmatrix}. \quad (2.12)$$

Diagonalizing this Hamiltonian gives the energy dispersion relations for π^* (conduction) band (+) and π (valence) band (-):

$$\begin{aligned} E^\pm(\mathbf{k}) &= \pm \gamma_0 |\alpha(\mathbf{k})| \\ &= \pm \gamma_0 \sqrt{3 + 2 \cos(\mathbf{k} \cdot \mathbf{a}_1) + 2 \cos(\mathbf{k} \cdot \mathbf{a}_2) + 2 \cos(\mathbf{k} \cdot (\mathbf{a}_2 - \mathbf{a}_1))} \\ &= \pm \gamma_0 \sqrt{1 + 4 \cos \frac{\sqrt{3} k_x a}{2} \cos \frac{k_y a}{2} 4 \cos^2 \frac{k_y a}{2}}. \end{aligned} \quad (2.13)$$

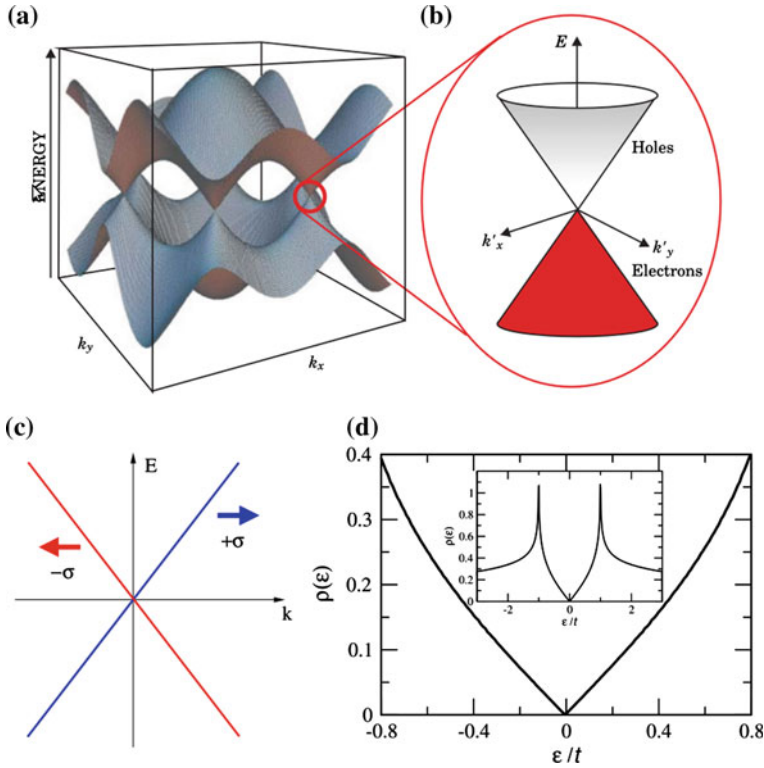


Fig. 2.3 Band structure of graphene (a), the zoom-in figure at close to K and K' points (b, c) and the density of state of graphene (d) (Figure is taken from [11])

This band structure is plotted in Fig. 2.3 with the symmetry between the conduction band and the valence band which touch at three K and K' points with zero density of state at this energy (Fig. 2.3d). Because of this, graphene is called gapless semiconductor or semi-metal. In neutral graphene, the Fermi level lie exactly at these points.

2.2.2 Low-Energy Dispersion

Because of the fact that they can only experimentally tune the Fermi level a small range (0.3 eV) about the touching points, this corresponds to a small variation around the K and K' points in momentum space. Therefore, it is sufficient to expand the energy dispersion in the vicinity of K and K' points by replacing $\mathbf{k} \rightarrow \mathbf{K}(\mathbf{K}') + \mathbf{k}$, which lets us write Eq. (2.12) in the form

$$\mathcal{H} = \hbar v_F (\eta \sigma_x k_x + \sigma_y k_y). \quad (2.14)$$

and Eq. (2.13) becomes

$$E_s(\mathbf{k}) = s\hbar v_F |\mathbf{k}|, \quad (2.15)$$

where $v_F = \sqrt{3}\gamma_0 a/2\hbar$ is the electronic group velocity, $\eta = 1(-1)$ for $K(K')$ points, $s = \pm 1$ is the band index (+1 for conduction band and -1 for valence band) and the Pauli matrices are defined as usual:

$$\sigma_x = \begin{pmatrix} 0 & 1 \\ 1 & 0 \end{pmatrix}, \quad \sigma_y = \begin{pmatrix} 0 & -i \\ i & 0 \end{pmatrix}, \quad \sigma_z = \begin{pmatrix} 1 & 0 \\ 0 & -1 \end{pmatrix}. \quad (2.16)$$

Equation (2.14) is almost the same the Dirac equation for the massless fermions in quantum electrodynamics except for the fact that the Pauli matrices here represent the sublattice degrees of freedom instead of spin and the speed of light c is replaced by graphene velocity $v_F \simeq c/300$. Therefore, the sublattice degrees of freedom and the touching points are called *pseudospin* and *Dirac point*, respectively.

The linear energy dispersion in Eq. (2.15) leads to the fact that total density of states is directly proportional to energy and carrier density is proportional to energy squared.

Indeed,

$$\rho(E) = \frac{1}{L^2} \sum_{\mathbf{k}} \delta(E - E(\mathbf{k})) = \int g_s g_v \frac{2\pi k dk}{(2\pi)^2} \delta(E - E(k)) = \frac{2|E|}{\pi \hbar^2 v_F^2} \quad (2.17)$$

which is plotted in Fig. 2.3d, where $g_s = 2$ and $g_v = 2$ account for spin and valley degeneracies, respectively. The carrier density is given by

$$n(E) = \frac{1}{L^2} \sum_{|\mathbf{k}| \leq k_F} g_s g_v = g_s g_v \frac{k_F^2}{4\pi} = \frac{E^2}{\pi \hbar^2 v_F^2} \quad (2.18)$$

To find the eigenstates of Dirac Hamiltonian (2.14), it is useful to write this Hamiltonian in the term of momentum direction θ_k

$$\mathcal{H}_\eta(\mathbf{k}) = \hbar v_F k \begin{pmatrix} 0 & e^{-i\eta\theta_k} \\ e^{+i\eta\theta_k} & 0 \end{pmatrix} \quad (2.19)$$

where $\theta_k = \arctan(k_y/k_x)$. This Hamiltonian has the eigenvalues given by Eq. (2.15) and the eigenfunctions

$$|\Psi_{\eta,s}(\mathbf{k})\rangle = \frac{1}{\sqrt{2}} \begin{pmatrix} 1 \\ s e^{i\eta\theta_k} \end{pmatrix}. \quad (2.20)$$

Next, we are going to find eigenvalues of the helicity operator (a very important feature of Dirac particle) which here is defined as:

$$\hat{h} = \hat{\sigma} \cdot \frac{\mathbf{p}}{|\mathbf{p}|}. \quad (2.21)$$

where $\mathbf{p} = \hbar \mathbf{k}$ is the electron momentum operator.

In order to do that, it is convenient to exchange the spinor components at the K' point (for $\eta = -1$) [12],

$$|\Psi^{\mathbf{K}}(\mathbf{k})\rangle = \begin{pmatrix} c_A(\mathbf{k}) \\ c_B(\mathbf{k}) \end{pmatrix}, \quad |\Psi^{\mathbf{K}'}(\mathbf{k})\rangle = \begin{pmatrix} c_B(\mathbf{k}) \\ c_A(\mathbf{k}) \end{pmatrix} \quad (2.22)$$

i.e., to invert the role of the two sublattices. In this case, the effective low-energy Hamiltonian in Eq. (2.14) may be represented as

$$\mathcal{H}^\eta(\mathbf{k}) = \eta \hbar v_F (\sigma_x k_x + \sigma_y k_y) = \hbar v_F \tau^z \otimes \vec{\sigma} \cdot \vec{k}. \quad (2.23)$$

where τ are Pauli matrices representing the valley degree of freedoms called *valley pseudospin*. Using Eqs. (2.23) and (2.21)

$$\mathcal{H}^\eta(\mathbf{k}) = \eta \hbar v_F k \hat{h} \quad (2.24)$$

we find that helicity operator commutes with the Hamiltonian, the projection of the pseudospin is a well-defined conserved quantity which can be either positive or negative, corresponding to pseudospin and momentum being *parallel* or *antiparallel* to each other. The band index s , which describes the valence and conduction bands, is therefore entirely determined by the chirality and the valley pseudospin, and one finds

$$s = \eta h \quad (2.25)$$

which help us find out that chirality changes sign from conduction band to valence band and from K to K' points. The fact that pseudospin is blocked with momentum has a strong influence in many of the most intriguing properties of graphene. For example, for an electron to backscatter (i.e. changing \mathbf{p} to $-\mathbf{p}$) it needs to reverse its pseudospin (see Fig. 2.3c). So backscattering is not possible if the Hamiltonian is not perturbed by a term which flips the pseudospin. This makes electrons in graphene insensitive to long-range scatterers. This characteristic manifests itself in some phenomena such as Klein tunneling or WAL [13, 14]. Klein tunneling [15] is a spectacular manifestation of the Dirac fermions physics which describes that when the Dirac charge crosses a tunneling barrier, the incoming electron is partially or totally transmitted depending on the incident angle of the incoming wavepacket. Especially, the barrier always remains perfectly transparent for angles close to normal incidence regardless of the height and width of the barrier, standing as a feature unique

to massless Dirac fermions and being completely different from the usual charge whose transmission probability decays exponentially with the barrier width. Klein tunneling has been studied theoretically and it shows that for long range potentials which preserve AB symmetry and prohibits intervalley scattering, the backscattering is totally suppressed.

In next section, we will discuss in more detail the effect of special band structure and pseudospin-momentum coupling on the transport properties of graphene.

2.3 Electronic and Transport Properties of Disordered Graphene

The disorder in graphene sample is practically an inevitable factor in any experiment. In some ways, artificial disorders are also tools to engineer, functionalize the materials. For instance, pure semiconductors are poor conductors and poor insulators. However, their magnificent properties have been achieved by functionalization using n - and p -type dopants, leading to p - n junctions, transistors, junction lasers, light-emitting diodes, and an entire technological revolution.

Similarly to semiconductors, in spite of having unique properties such as superb mechanical strength and carrier mobility, pristine graphene is not useful for practical applications because of its low carrier density, zero band gap, and chemical inertness. The lack of electronic gap in pristine graphene is an issue that has to be overcome to achieve high I_{on}/I_{off} current ratio in graphene-based field-effect devices. Therefore, it is important to study the disorder effect on the electronic properties of graphene not only to conquer its detrimental effects but also use artificial defects to functionalize graphene devices.

The study of transport properties is at the heart of graphene research. Experiments show that the conductivity (down to a few Kelvin) is almost constant close to the Dirac point, $\sigma \sim 2 - 5e^2/h$, and weakly dependent on the value of the charge mobility [15–18]. On the theoretical side, within the self-consistent Born approximation (SCBA) the semiclassical part of the conductivity due to short range disorder is found to be $\sigma^{min} = 4e^2/\pi h$ which is known as the quantum limited conductivity of graphene in clean limit [19].

However, transport properties of graphene are strongly dependent on the nature of possible sources of disorder. There are many kinds of disorders in graphene, some are long-range disorders such as Coulomb interactions of charged impurities in the substrate, electron-hole puddle, long range strain deformations, distortion of graphene structure, etc. Other forms are related to the sp^3 defects such as epoxide defects, the absorption of hydroxyl, hydrogen, fluorine, etc. on graphene (See Fig. 2.4). Finally topological disorders which keep the sp^2 hybridization of graphene but change the hexagonal structure, involve structural point defects and line defects or GBs.

The electronic properties of graphene are well described by the π -orbital tight-binding Hamiltonian in which the disorder in the real sample can be simulated by changing the on-site energies $\delta\epsilon$ of π -orbital. One of the simplest disorder model in

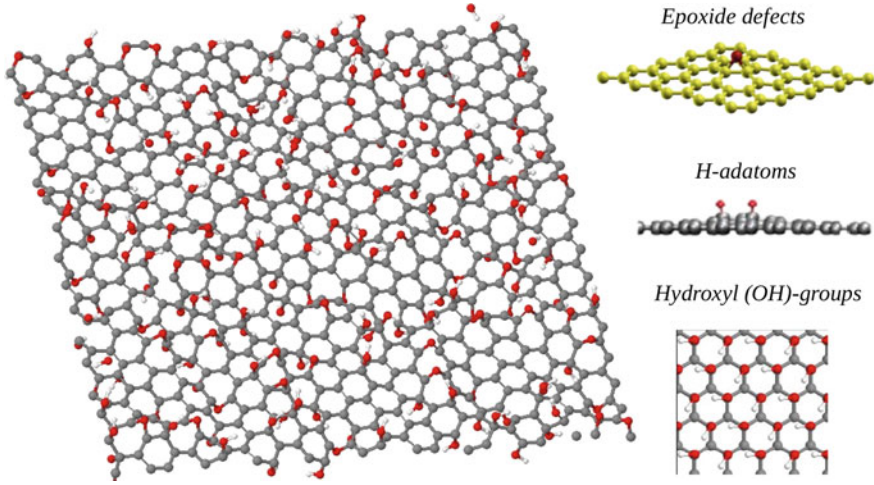
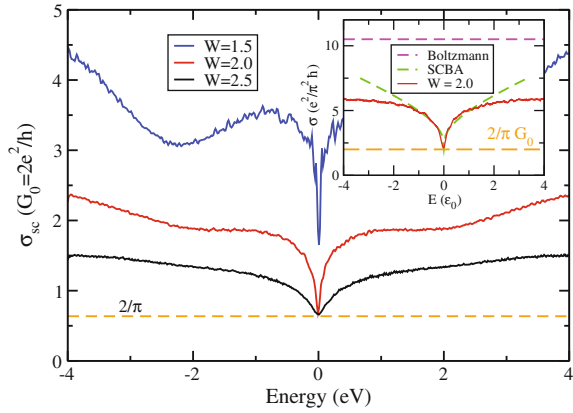


Fig. 2.4 Some kinds of sp^3 disorder in graphene

Fig. 2.5 Main frame: The semiclassical conductivity for Anderson disorder. *Inset* the comparison of Kubo-Greenwood approach with the Boltzmann and self-consistent Born approximation (Figure is taken from [20])



graphene is the short-range scattering potential, namely the Anderson disorder [20, 21]. This white noise uncorrelated disorder is introduced through random modulations of the onsite energies $\delta\epsilon \in [-W/2, W/2]\gamma_0$. This disorder could in principle mimic neutral impurities such as structural defects, dislocation lines, or adatoms, although the local geometry and chemical reactivity of defects and impurities actually demand for more sophisticated *ab initio* calculations if aiming at quantitative predictions.

Figure 2.5 shows the energy dependence of semiclassical conductivity from the Kubo formalism for some values of W (main frame) and the comparison with one from SCBA (inset). The results are in good agreement at low energy and close to the theoretically predicted minimum conductivity $\sigma^{min} = 4e^2/\pi h$. For higher energies, the agreement with SCBA is lost due to higher order deviations. Furthermore, the SCBA is not sufficient to describe such a system with all symmetries broken.

The role of disorder on WL and WAL in graphene has also been intensively investigated. From a general perspective, the conductance of a system can be viewed as the sum ($\mathcal{P}_{A \rightarrow B}$) over all probability amplitudes of propagating trajectories starting from one location A and going to another one B in real space, or more explicitly

$$G = \frac{2e^2}{h} \mathcal{P}_{A \rightarrow B} \quad (2.26)$$

$$\mathcal{P}_{A \rightarrow B} = \sum_i |\mathcal{A}_i|^2 + \sum_{i \neq j} \mathcal{A}_i \mathcal{A}_j^* \quad (2.27)$$

Here $\mathcal{A}_i = |\mathcal{A}_i| e^{i\Delta\varphi_i}$ is the propagation amplitude along the path i . The first term denotes the classical probability corresponding to semiclassical conductivity σ_{sc} while the second one is the interference term which gives the quantum correction $\delta\sigma(L)$ of the semiclassical result $\sigma(L) = \sigma_{sc} + \delta\sigma(L)$. For the majority of the trajectories the phase gains,

$$\Delta\varphi = \hbar^{-1} \int_A^B \mathbf{p} d\mathbf{l} \gg 1 \quad (2.28)$$

and the interference term vanishes. However, for some special trajectories with self-crossings, if we change the direction of propagation, $\mathbf{p} \rightarrow -\mathbf{p}$, $d\mathbf{l} \rightarrow -d\mathbf{l}$, the phase gains are the same, i.e. $\mathcal{A}_i \mathcal{A}_j^* = |\mathcal{A}_i|^2$, and quantum interference thus eventually enhance the probability of return to some origin. This contribution of quantum interferences gives rise to the increase of the quantum resistance, i.e. $\delta\sigma(L) < 0$, known as localization. There are two different scaling behaviors of localization: the WL with [10, 20, 22]

$$\delta\sigma(L) = -\frac{2e^2}{\pi h} \ln \left(\frac{L}{l_e} \right) \quad (2.29)$$

and strong localization described by

$$\sigma(L) \sim \exp \left(-\frac{L}{\xi} \right) \quad (2.30)$$

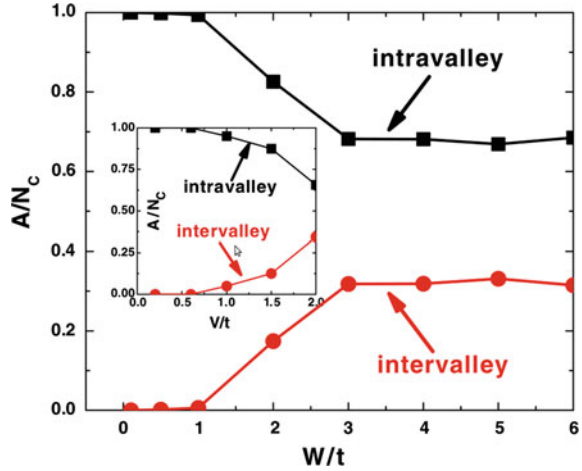
where L , l_e , and ξ denote the sample length, mean free path and the localization length, respectively.

However, we haven't considered the contribution of additional degrees of freedom such as spin or pseudospin in graphene. The detail calculations (for more details, see Ref. [10] and references therein) showed that these contributions can lead to the sign reversal of quantum correction of conductivity

$$\delta\sigma(L) = +\frac{2e^2}{\pi h} \ln \left(\frac{L}{l_e} \right) \quad (2.31)$$

which is the scalling law for WAL.

Fig. 2.6 The contribution from intra and intervalley scattering (Figure is taken from [23])



As mentioned above, the Dirac fermions in graphene are expected to exhibit the WAL behavior but another effect should also be involved to consider the whole picture, that is trigonal warping which is related to the momentum contribution from higher order into Eq. (2.15). The trigonal warping is predicted to suppress antilocalization and together with intervalley scattering, it restores the weak localization (WL) [13]. The crossovers from WAL to WL and the effect of disorders on intra- and intervalley scattering were studied in many Refs. [13, 14, 20, 23] in which the long range disorder is simulated by changing onsite energies $V_i = \sum_{j=1}^N \epsilon_j \exp[-(\mathbf{r}_i - \mathbf{R}_j)^2/(2\xi^2)]$ where ϵ_j are chosen at random within $[-\frac{W}{2}, \frac{W}{2}]$. These calculations show that the strength of local potential profile control the contribution of intra- and intervalley scatterings on the conductivity. Following the theoretical study in Ref. [23], the intravalley scattering dominates at small value of W ($W < \gamma_0$) and valley mixing strength was continuously enhanced from $W = \gamma_0$ to $W = 2\gamma_0$. The intervalley scattering contribution is large enough as $W > 2\gamma_0$ (See. Fig. 2.6). As a consequence, graphene exhibits the crossover from WAL to WL as W increase (See Fig. 2.7). Indeed, the positive magnetoconductance for the case $W = 2\gamma_0$ (top panels) agrees with the strong contribution of intervalley scattering, since all graphene symmetries have been broken. However by decreasing the disorder strength from $W = 2\gamma_0$ to $W = 1.5\gamma_0$ (bottom panels), WAL is indeed recovered given the reduction of intervalley processes.

Chemical absorption in graphene is usually related to oxidation or hydrogenation of graphene which are strongly invasive for electronic and transport properties and systematically drive graphene to a strong Anderson insulator [25]. The theoretical and experimental studies show that high coverage sp^3 formations which break local AB symmetry such as in hydrogenated or fluorinated graphene induce energy band gap in the high density limit. Especially, graphane, fully hydrogenated graphene, is predicted to be a stable semiconductor with the energy gap as large as 3.5 eV [26], some recent DFT calculations using the screened hybrid functional of Heyd, Scuseria,

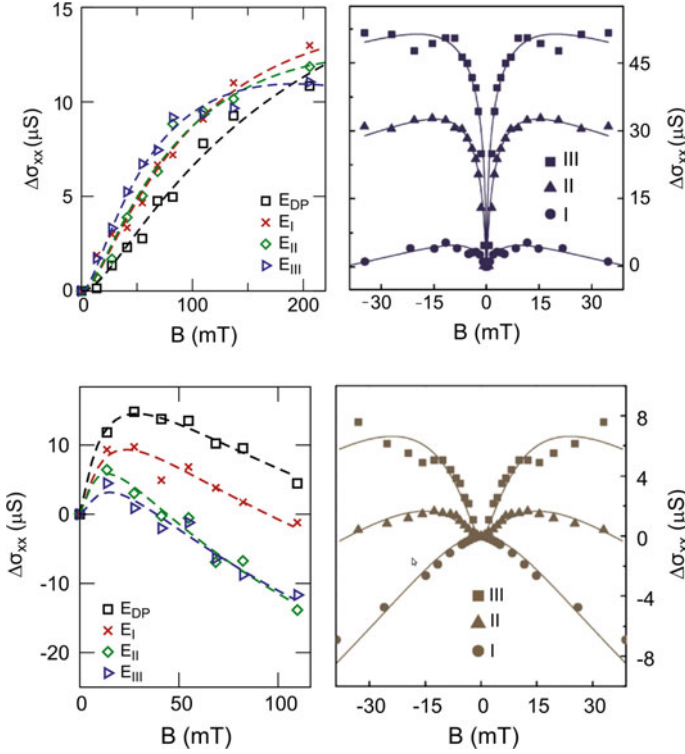


Fig. 2.7 Magnetoconductance for $W = 2\gamma_0$ (top panels) and $W = 1.5\gamma_0$ (bottom panels), the data is extracted from theoretical (left panels) and experimental (right panels) study (Figure is taken from [20])

and Ernzerhof (HSE) even gave a larger energy gap up to 4.5 eV for graphane and 5.1 eV for fluorographene (fully fluorinated graphene) (See Fig. 2.8). The case of low coverage of hydrogen is more interesting with the transport properties strongly depending on the absorbing position. Theory predicted that graphene exhibits WL for the compensated case (hydrogen absorbs equally in two sublattices) whereas the quantum interferences and localizations are suppressed if hydrogen defects are restricted to one of the two sublattices [20]. The analogy of transport properties of chemical absorptions and long-range potentials have also been studied. As one can see in Fig. 2.9, some chemical absorptions at bridge position such as epoxide defects which preserve local AB symmetry induce energy-dependent elastic scattering time ($\tau_e(E)$) resembling the case of long range impurities with small onsite potential depth, whereas some adsorbates at the top position such as hydrogen or fluorine defects which break local sp^2 and AB symmetry give rise to elastic scattering time resembling the case of strong long range potentials. These are due to the fact that transport time behavior is controlled by the contribution of inter- and intravalley scatterings which are mainly determined by the breaking of AB symmetry.

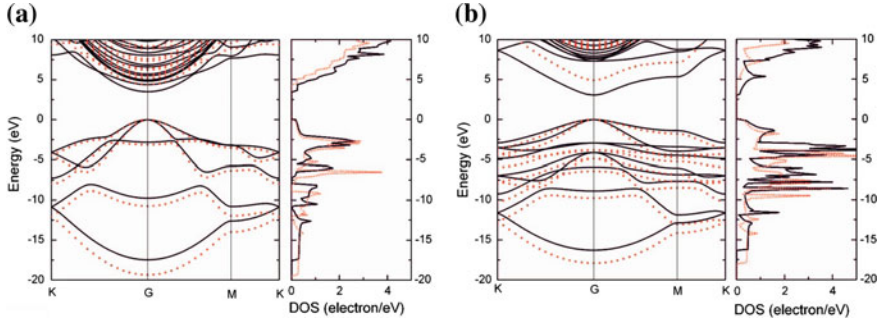


Fig. 2.8 The electronic band structure and projected density of states in the vicinity of the band gap for graphane (a) and fluorographane (b) (Figure is taken from [24])

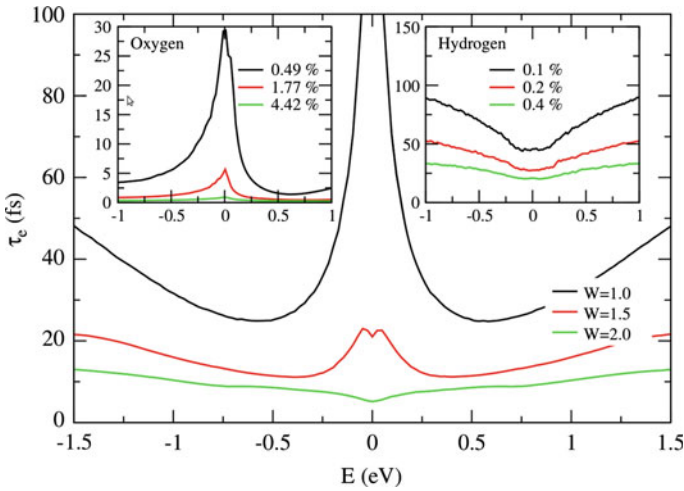


Fig. 2.9 Elastic scattering time (τ_e) versus energy for three different long-range potential strengths W . *Left inset* τ_e for various densities of epoxide defects. *Right inset* τ_e for various densities of hydrogen defects (Figure is taken from [20])

In particular, the formation of sp^3 hybridizations or monovacancies in graphene can give rise to local sublattice imbalances and thus induce local magnetic moment according to Lieb's theorem [27]. The existence of magnetism in graphene as well as magnetism-dependent transport properties have been studied in many Refs. [28–30]. Especially, when half of the hydrogen in graphane sheet is removed, the resulting semihydrogenated graphene (graphone) becomes a ferromagnetic semiconductor with a small indirect gap [31].

Structural point defects usually exist in various geometrical forms in graphene. They can be obtained for instance when irradiating graphene samples. In this kind of graphene, the disorder is created locally in the sample by locally changing the hexagonal structure such as removing a carbon atom from the graphene sheet (monovacancy)

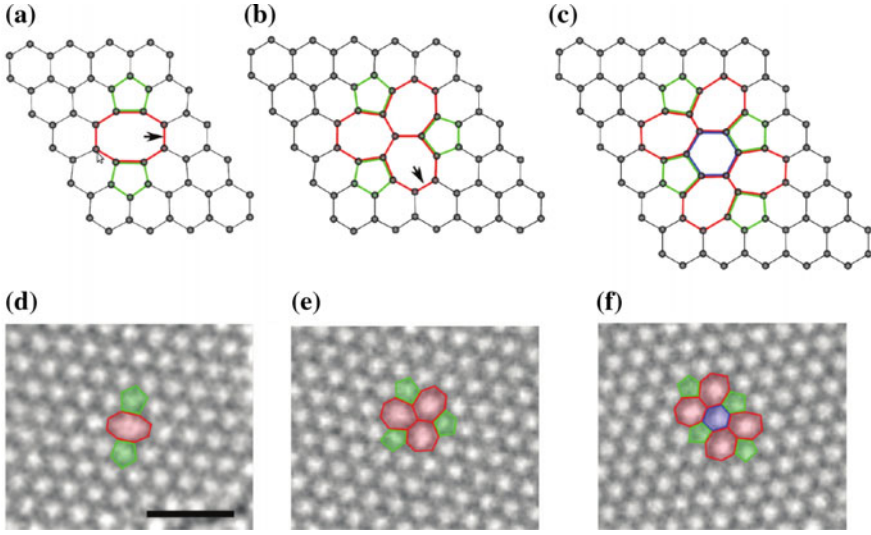


Fig. 2.10 Some structural point defects (*top panels*) and their experimental TEM images (*bottom panels*) (Figure is taken from [35])

or rotating a pair of carbon 90° in graphene plane (Stone-Wales defects). Some studies [32] showed that monovacancies are very mobile and unstable, recombining in di- or multivacancies or local structures with some nonhexagonal rings which are more stable. The transport properties of graphene under the influence of structural point defects such as vacancies, divacancies, Stone-Wales defects, 585 divacancies (See Fig. 2.10), etc. have been now widely studied [33, 34], revealing interesting features such as electron-hole transport asymmetry [33, 34] due to the presence of defect-induced resonances. Under electron irradiation, graphene changes from pristine form to structural defects and finally to a new two-dimensional amorphous carbon lattice [36] which is composed of sp^2 -hybridized carbon atoms, arranged as a random tiling of the plane with polygons including four-membered rings. Most theoretical studies [37, 38] found out that there is a huge increase of the density of state at the charge neutrality point in this amorphous graphene and these states are localized, suggesting that the amorphous graphene is an Anderson insulator. However, using a stochastic quenching method, Ref. [39] claimed that “*we predict a transition to metallicity when a sufficient amount of disorder is induced in graphene...*”. In Chap. 4, by using Kubo-Greenwood calculations, we show that this conclusion is misleading and similar results have also been obtained recently in Ref. [40].

Although possessing many excellent electrical, optical and mechanical properties, perfect graphene (single-crystal graphene) is only fabricated in small size by exfoliation method. So far, the most promising approach for the mass production of large-area graphene is CVD, which results in a graphene with many line defects (See Fig. 2.11) or Poly-G. This polycrystallinity arises due to the nucleation of growth sites at random positions and orientations during the CVD process. In order to

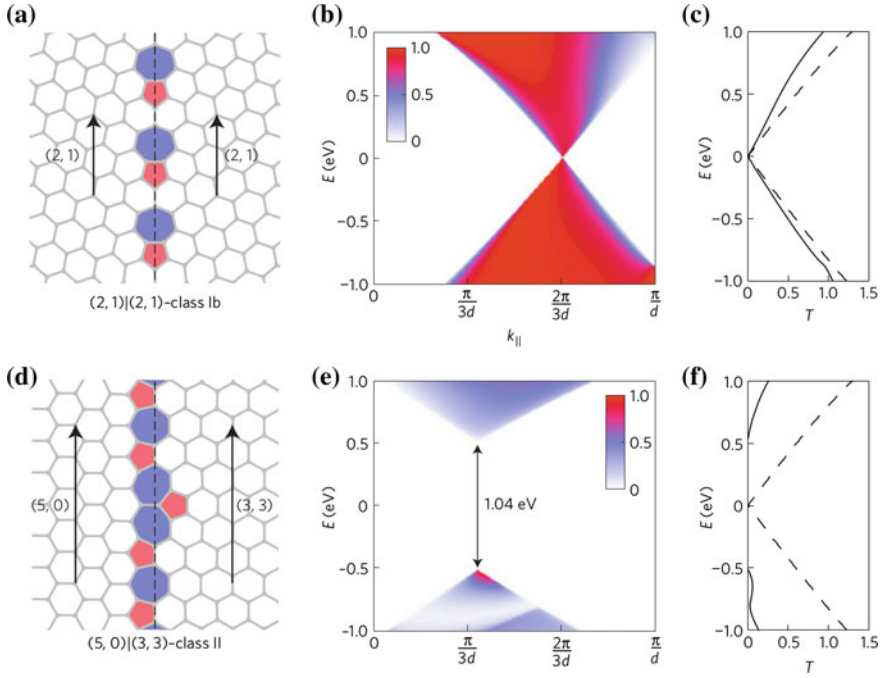


Fig. 2.11 Two classes of electron transport through GBs (Figure is taken from [41])

accommodate the lattice mismatch between misoriented grains, the GBs in Poly-G are made up of a variety of non-hexagonal carbon rings, which can act as a source of scattering during charge transport. Because of its potential for applications, the transport properties of Poly-G are the subject of intense research. Some calculations showed that the effect of GBs on the carrier transport differ depending on the GB geometry (See Fig. 2.11) resulting in a tunable mobility (tunable transport gaps) [41] which allows to control charge currents without the need to introduce bulk band gaps in graphene. In so-called class I GBs (top panels of Fig. 2.11), including all symmetrical GBs, the projected periodicities of the lattice on each side match in a way that allows carriers to cross freely even at the Dirac point. In class II GBs (bottom panels of Fig. 2.11), no such momentum-conserving transmission is possible, except for carriers with much higher energy. Another calculation pointed out that some line defects can play the role as semitransparent “valley filter”. It was found that carriers arriving at this line defect with a high angle of incidence are transmitted with a valley polarization near 100% [42]. Many experimental works have studied the transport properties of Poly-G and showed that the GBs generally degrade the electrical performance of graphene [43, 44] and specifically, the interdomain connectivity plays an important role to control the electrical properties of Poly-G, with the electrical conductance that can be improved by one order of magnitude for GBs with better interdomain connectivity [43]. However, just a few theoretical works have studied

the complex structures of GBs and corresponding electronic transport. In Chap. 4, by using molecular dynamics, we simulate the Poly-G with variable grain sizes, and tunable interdomain connectivities, and report on a scaling law for transport properties of Poly-G, which points out that the semiclassical conductivity and mean free path are directly proportional to grain size and both are strongly affected by grain connectivity. However, as pointed out in our next calculation, the GB resistivity for non-contaminated Poly-G is very low compared to the experimental results [43, 45, 46]. The explanation for this problem is that the GBs which contain many nonhexagonal structure have greater chemical reactivity [47] and are usually functionalized by many different types of chemical adsorbates. This has been confirmed in several experiments [48, 49]. By using the numerical simulations we report on the role played by chemical adsorbates on GBs in charge transport in Chap. 4.

2.4 Spin Transport in Graphene

Beside many interesting electronic properties, graphene is also considered to be a promising candidate for spintronic applications. The spin relaxation time in intrinsic graphene is expected to be very long and therefore graphene has high potential as a spin-conserving system which can transmit spin-encoded information across a device with high fidelity. The underlying reason for long spin relaxation time is the low hyperfine interactions of the spin with the carbon nuclei (natural carbon only contains 1 % ^{13}C) and the weak SOC due to the low atomic number [50]. The theoretical prediction showed that the spin relaxation time in graphene is in the order of microseconds. However, the reported experimental spin relaxation times remain several orders of magnitude lower than the original theoretical predictions.

Because spin relaxation based on the graphene intrinsic SOC could not give a convincing explanation, other extrinsic sources of spin relaxation are believed to come into play. Proposals to explain the unexpectedly short spin relaxation times include spin decoherence due to interactions with the substrate, the extrinsic SOC induced by impurities, adatoms, ripples or corrugations, etc. which will be reviewed below. The puzzling controversy of the spin relaxation mechanism will be mentioned in the next section.

2.4.1 Spin-Orbit Coupling in Graphene

In order to derive the SOC term in the Hamiltonian, it is necessary to start from the relativistic Hamiltonian, the Dirac equation: $H|\psi\rangle = E|\psi\rangle$ with

$$H = \begin{pmatrix} 0 & c\mathbf{p}\cdot\boldsymbol{\sigma} \\ c\mathbf{p}\cdot\boldsymbol{\sigma} & 0 \end{pmatrix} + \begin{pmatrix} mc^2 & 0 \\ 0 & -mc^2 \end{pmatrix} + V \quad (2.32)$$

and where the wave function is a two-components spinor: $|\psi\rangle = (\psi_A, \psi_B)^T$. From the Dirac equation we obtain two equations for spinor components:

$$\psi_B = \frac{c\mathbf{p}\cdot\boldsymbol{\sigma}}{E - V + mc^2}\psi_A \quad (2.33)$$

$$\mathbf{p}\cdot\boldsymbol{\sigma}\frac{c^2}{E - V + mc^2}\mathbf{p}\cdot\boldsymbol{\sigma}\psi_A = (E - V - mc^2)\psi_A \quad (2.34)$$

In the nonrelativistic limit, the lower component ψ_B is very small compared to the upper component ψ_A . Indeed, with the relativistic energy $E = mc^2 + \epsilon$ and $V \ll mc^2$, Eq. (2.33) drive us to

$$\psi_B = \frac{\mathbf{p}\cdot\boldsymbol{\sigma}}{2mc}\psi_A \ll \psi_A \quad (2.35)$$

and Eq. (2.34) leads us to the Schrodinger equation.¹

$$\left(\frac{p^2}{2m} + V\right)\psi_A = \epsilon\psi_A \quad (2.36)$$

In other words, in the first order of (v/c) , ψ_A is equivalent to the Schrodinger wave function ψ . In order to obtain the analogy of ψ_A and ψ at higher order of (v/c) , we use the normalization characteristic of the wave function

$$\int (\psi_A^\dagger\psi_A + \psi_B^\dagger\psi_B) = 1 \quad (2.37)$$

To first order, using Eq. (2.35), this gives

$$\int \psi_A^\dagger \left(1 + \frac{p^2}{4m^2c^2}\right) \psi_A = 1 \quad (2.38)$$

Apparently, to have a normalized wave function, we should use $\psi = \left(1 + \frac{p^2}{8m^2c^2}\right)\psi_A$. Substituting this into the Dirac equation, and using the expansion $\frac{c^2}{E - V + mc^2} \simeq \frac{1}{2m} \left(1 - \frac{\epsilon - V}{2mc^2} + \dots\right)$, we obtain, after some rearrangement, the Pauli equation

$$\left(\frac{p^2}{2m} + V - \frac{p^4}{8m^3c^2} - \frac{\hbar}{4m^2c^2}\boldsymbol{\sigma}\cdot\mathbf{p} \times \nabla V + \frac{\hbar^2}{8m^2c^2}\nabla^2 V\right)\psi = \epsilon\psi \quad (2.39)$$

the first and the second terms are the usual terms in the Hamiltonian, the third term is simply a relativistic correction to the kinetic energy. The fourth term is the SOC term and the final term give the energy shift due to the potential.

¹Using $(\boldsymbol{\sigma}\cdot\mathbf{A})(\boldsymbol{\sigma}\cdot\mathbf{B}) = \mathbf{A}\cdot\mathbf{B} + i\boldsymbol{\sigma}\cdot(\mathbf{A} \times \mathbf{B})$.

Hereafter, I will derive the SOC term in the more intuitive way which gives the physical meaning of SOC interaction. Suppose an electron is moving with velocity \mathbf{v} in an electric field $-e\mathbf{E} = -\nabla V$. This electric field might be induced by the potential V of the adatoms or the substrate. In relativistic theory, this moving electron feels a magnetic field $\mathbf{B} = -\frac{\mathbf{v} \times \mathbf{E}}{c}$ in its rest frame. The interaction between this magnetic field and the electron spin leads to the potential energy term:

$$V_{\mu_s} = -\mu_s \mathbf{B} = -\frac{g_s \mu_B}{2ec} \boldsymbol{\sigma} \cdot \mathbf{v} \times \nabla V = -\frac{g_s \hbar}{4m^2 c^2} \boldsymbol{\sigma} \cdot \mathbf{p} \times \nabla V = -\frac{\hbar}{2m^2 c^2} \boldsymbol{\sigma} \cdot \mathbf{p} \times \nabla V \quad (2.40)$$

This results is twice the SOC term in Pauli equations. Actually, this was the major puzzle, until it was pointed out by Thomas [51] that this argument overlooks a second relativistic effect that is less widely known, but is of the same order of magnitude: electric field \mathbf{E} causes an additional acceleration of the electron perpendicular to its instantaneous velocity \mathbf{v} , leading to a curved electron trajectory. In essence, the electron moves in a rotating frame of reference, implying an additional precession of the electron, called the Thomas precession. As a result, the electron “sees” the magnetic field at only one-half the above value

$$\mathbf{B} = -\frac{\mathbf{v} \times \mathbf{E}}{2c} \quad (2.41)$$

which leads to the full SOC term

$$V_{SOC} = -\frac{\hbar}{4m^2 c^2} \boldsymbol{\sigma} \cdot \mathbf{p} \times \nabla V \quad (2.42)$$

Now let's rewrite the SOC term in form of the SOC force \mathbf{F}

$$H_{SOC} = \alpha (\mathbf{F} \times \mathbf{p}) \cdot \mathbf{s} = -\alpha (\mathbf{s} \times \mathbf{p}) \cdot \mathbf{F} \quad (2.43)$$

where α is an undetermined parameter. Here we use \mathbf{s} instead of $\boldsymbol{\sigma}$ to represent the spin degree of freedom to avoid any misunderstanding with pseudospin in graphene.

If we consider intrinsic graphene, the inversion symmetry dictates the electric field (force) in plane and this SOC is called intrinsic SOC. Because of structure's mirror symmetry with respect to any nearest-neighbor bond (See Fig. 2.12a), the nearest-neighbor intrinsic SOC is zero, while the next nearest-neighbor intrinsic SOC is nonzero. According to symmetry,

$$H_I = i\gamma_2 \left(\mathbf{F}_{//} \times d_{ij} \right) \cdot \mathbf{s} = \frac{2i}{\sqrt{3}} V_I \mathbf{s} \cdot (\hat{\mathbf{d}}_{kj} \times \hat{\mathbf{d}}_{ik}) \quad (2.44)$$

where γ_2 and V_I are undetermined parameters, and $\hat{\mathbf{d}}_{ij}$ is the unit vector from atom j to its next-nearest neighbors i , and k is the common nearest neighbor of i and j

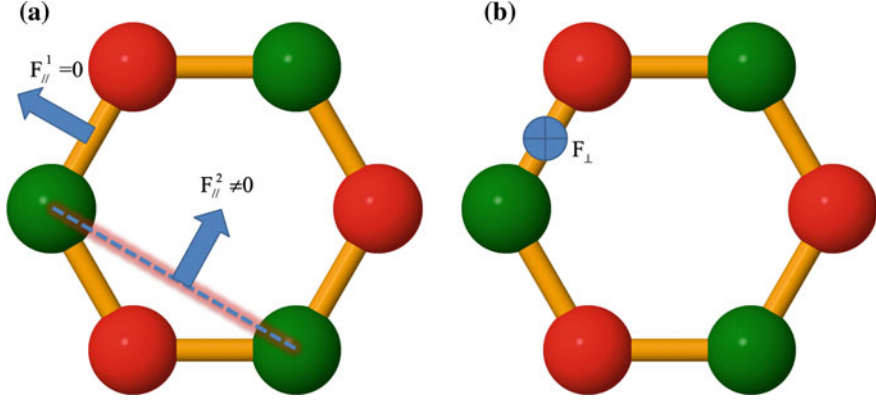


Fig. 2.12 SOC in graphene: **a** Intrinsic SOC forces. **b** Rashba SOC force

In the presence of the out of plane electric field (See Fig. 2.12b) which can originate from a gate voltage or charged impurities in the substrate, adatoms, etc., the band structure of graphene changes. This external electric field breaks spatial inversion symmetry and causes a nearest-neighbor extrinsic SOC. This SOC is Rashba SOC and has the form

$$H_R = i\gamma_1 (\mathbf{s} \times \hat{\mathbf{d}}_{ij}) \cdot F_{\perp} \mathbf{e}_z = iV_R \hat{\mathbf{z}} \cdot (\mathbf{s} \times \hat{\mathbf{d}}_{ij}) \quad (2.45)$$

where j is the nearest-neighbor of i and γ_1 and V_R are undetermined parameters.

Finally, we get the TB Hamiltonian:

$$\mathcal{H} = -\gamma_0 \sum_{\langle ij \rangle} c_i^{\dagger} c_j + \frac{2i}{\sqrt{3}} V_I \sum_{\langle\langle ij \rangle\rangle} c_i^{\dagger} \mathbf{s} \cdot (\hat{\mathbf{d}}_{kj} \times \hat{\mathbf{d}}_{ik}) c_j + iV_R \sum_{\langle ij \rangle} c_i^{\dagger} \hat{\mathbf{z}} \cdot (\mathbf{s} \times \hat{\mathbf{d}}_{ij}) c_j \quad (2.46)$$

By performing Fourier transformations, we obtain the low energy effective Hamiltonian around the Dirac point in the basis $\{|A\rangle, |B\rangle\} \otimes \{|\uparrow\rangle, |\downarrow\rangle\}$

$$h(\mathbf{k}) = h_0(\mathbf{k}) + h_R(\mathbf{k}) + h_I(\mathbf{k}) \quad (2.47)$$

where

$$\begin{aligned} h_0(\mathbf{k}) &= \hbar v_F (\eta \sigma_x k_x + \sigma_y k_y) \otimes 1_s \\ h_R(\mathbf{k}) &= \lambda_R (\eta [\sigma_x \otimes s_y] - [\sigma_y \otimes s_x]) \\ h_I(\mathbf{k}) &= \lambda_I \eta [\sigma_z \otimes s_z] \end{aligned} \quad (2.48)$$

with Fermi velocity $v_F = \frac{3}{2}\gamma_0$, Rashba SOC $\lambda_R = \frac{3}{2}V_R$ and intrinsic SOC $\lambda_I = 3\sqrt{3}V_I$ [52].

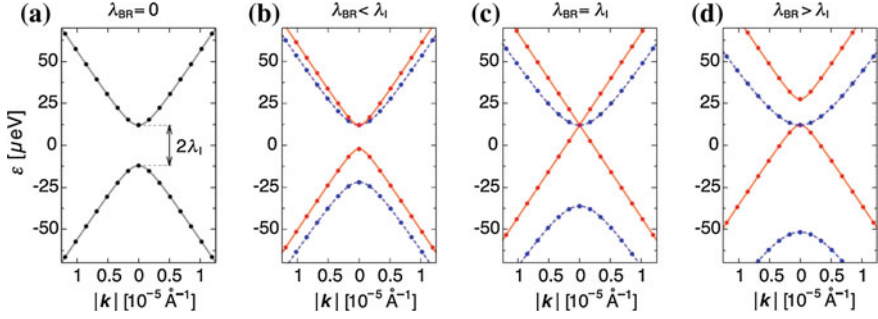


Fig. 2.13 Electronic bandstructure of graphene with SOC (Figure is taken from [53])

The remarkable thing about SOC in graphene is that the SOC terms are momentum-independent. The spin directly couples with pseudospin instead of momentum as in conventional metals or semiconductors, the usual SOC term ($\mathbf{k} \times \mathbf{s}$) is small and can be disregarded.

Diagonalizing the Hamiltonian in Eq. (2.47) gives the electronic bands close to the Dirac point [53, 54]:

$$\epsilon_{\mu\nu}(\mathbf{k}) = \mu\lambda_R + \nu\sqrt{(\hbar v_F k)^2 + (\lambda_R - \lambda_I)^2} \quad (2.49)$$

where μ and $\nu = \pm 1$ are band indexes.

If we consider intrinsic graphene, the Rashba SOC is vanishingly small, the intrinsic SOC opens a gap $\Delta = 2\lambda_I$ (See Fig. 2.13a). When Rashba SOC is turned on by inversion symmetry breaking (effect from the substrate, the electric field, the corrugations, etc.), the competition of Rashba and intrinsic SOC leads to gap closing. The gap remains finite $\Delta = 2(\lambda_I - \lambda_R)$ for $0 < \lambda_R < \lambda_I$ (Fig. 2.13b). For $\lambda_R > \lambda_I$ the gap closes and the electronic structure is that of a zero gap semiconductor with quadratically dispersing bands (Fig. 2.13d).

The eigenfunctions corresponding to the eigenvalues in Eq. (2.49) are

$$\psi_{\mu\nu}(\mathbf{k}) = \left(\chi_- |\eta e^{-i\eta\varphi} \left[\frac{\epsilon_{\mu\nu} - \lambda_I}{\nu \hbar v_F k} \right]^\eta, 1 \rangle + \mu \chi_+ |-i\eta e^{-i(1+\eta)\varphi}, i e^{-i\varphi} \left[\frac{\lambda_I - \epsilon_{\mu\nu}}{\nu \hbar v_F k} \right]^\eta \rangle \right) / C_{\mu\nu}$$

with $\tan \varphi = k_y/k_x$ and the normalization constant [53] $C_{\mu\nu} = \sqrt{2} \left(1 + \left[\frac{\lambda_I - \epsilon_{\mu\nu}}{\hbar v_F k} \right]^{2\eta} \right)^{1/2}$. The expectation value of the spin [53, 54],

$$\mathbf{s}_{\mu\nu}(\mathbf{k}) = \frac{\hbar v_F (\mathbf{k} \times \hat{\mathbf{z}})}{\sqrt{(\hbar v_F k)^2 + (\lambda_I - \mu\lambda_R)^2}} = \frac{\hbar v_F k}{\sqrt{(\hbar v_F k)^2 + (\lambda_I - \mu\lambda_R)^2}} \mathbf{n}(\mathbf{k}) \quad (2.50)$$

where $\mathbf{n}(\mathbf{k}) = (\sin\varphi, -\cos\varphi, 0)$ is the unit vector along the spin direction, called spin vector.

The remarkable characteristic of spin in spin-orbit coupled graphene in Eq. (2.50) is that it is polarized in-plane and perpendicular to electron momentum \mathbf{k} . The magnitude of spin polarization \mathbf{s} vanishes when $k \rightarrow 0$. The Chap. 5 will show that these behaviors are due to the fact that spin and pseudospin are strongly coupled close to the Dirac point where the coupling between pseudospin and momentum is zero because of the destructive interference between the three nearest-neighbor hopping paths. And this leads to the spin-pseudospin entanglement, the component of new spin relaxation mechanism that plays a major role in spin relaxation at the Dirac point in ultra clean graphene.

In the case of high energy $\hbar v_F k \gg \lambda_R + \lambda_I$, the pseudospin is mainly controlled by momentum via $h_0(\mathbf{k})$ and aligns in the same direction with momentum (in plane). Spin is dictated by pseudospin via $h_R(\mathbf{k})$, as a consequence, spin polarization for a certain momentum in Eq. (2.50) saturates to 1. By successive unitary rotation of $h(\mathbf{k})$ first into the eigenbasis of $h_0(\mathbf{k})$ and then into the spin basis with respect to the direction $\mathbf{n}(\mathbf{k})$ an effective Bychkov-Rashba-type 2×2 Hamiltonian can be obtained for both holes and electrons [9],

$$\tilde{h}(\mathbf{k}) = \nu(\hbar v_F k - \lambda_I) - \nu \lambda_R \mathbf{n}(\mathbf{k}) \cdot \mathbf{s} \quad (2.51)$$

The analogy of the second term in above equation and the original Bychkov-Rashba Hamiltonian in semiconductor heterostructures $H_{\mathbf{k}} = \hbar \boldsymbol{\Omega}(\mathbf{k}) \cdot \mathbf{s} / 2$ shows that SOC coupling in graphene effectively acts on the electrons spin as an in-plane magnetic field of constant amplitude but perpendicular to \mathbf{k} . In this effective field the spin precesses with a frequency and a period of [9]

$$\Omega = \frac{2\lambda_R}{\hbar}, \quad T_\Omega = \frac{\pi\hbar}{\lambda_R} \quad (2.52)$$

These results will be obtained again in Chap. 5 with the numerical calculations of the real-space order N method implemented for spin. Furthermore, we will point out that this result is only valid at high energy. At low energy the spin-pseudospin entanglement comes into play and creates a more complicated picture.

The magnitude of SOC interactions is also a matter of large concern. It is a crucial factor to determine not only quantitatively spin relaxation but also the mechanism at play. The numerical estimates for intrinsic SOC λ_I in graphene remains rather controversial. At the beginning, Kane and Mele [56] estimated the value of $100 \mu\text{eV}$. This optimistic estimate was drastically reduced by Min et al. [57] to the value of $0.5 \mu\text{eV}$ by using microscopic TB model and second-order perturbation theory. This value was later confirmed by Huertas-Hernando et al. [50] with TB model and Yao et al. [58] with first-principles calculations. A density functional calculation of Boettger and Trickey [59], using a Gaussian-type orbital fitting function methodology, gave $2 \mu\text{eV}$. Three Refs. [50, 57, 58] gave the same value of λ_I , but these calculations only involved the SOC induced by the coupling of the p_z orbitals (forming

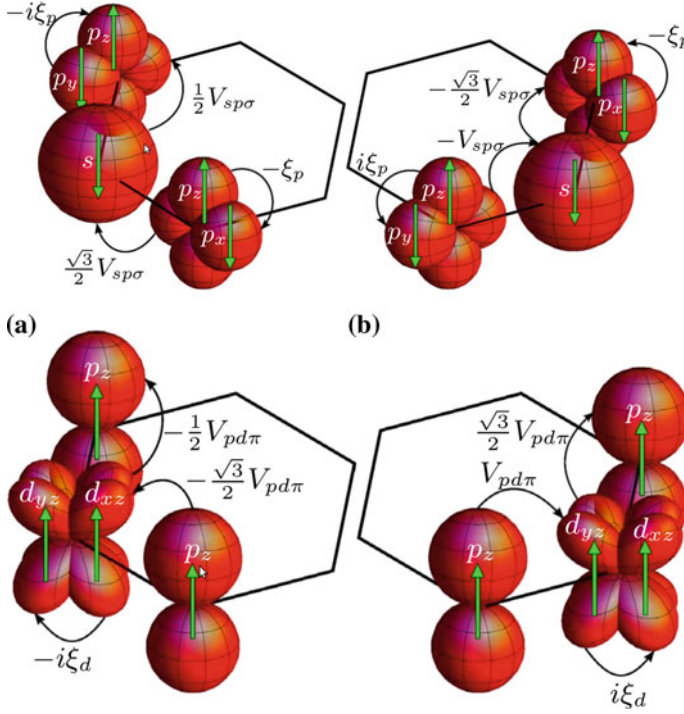


Fig. 2.14 Two possible hopping paths through s and p orbitals (*top panels*) and through d orbital (*bottom panels*) lead to the first and the second terms, respectively in Eq. (2.53) (Figure is taken from [55])

the π bands) to the s orbitals (forming the σ band). However, as pointed out in Ref. [55], the coupling of the p_z orbitals to the d orbitals (See Fig. 2.14) dominates the SOC at $K(K')$. Due to a finite overlap between the neighboring p_z and d_{xz} , d_{yz} orbitals, the intrinsic splitting λ_I is linearly proportional to the spin-orbit splitting of the d states, ξ_d (orbitals higher than d have a smaller overlap and contribute less). In contrast, due to the absence of the direct overlap between the p_z and σ -band orbitals, the usually considered spin-orbit splitting [50, 57, 58] induced by the $\sigma - \pi$ mixing depends only quadratically on the spin-orbit splitting of the p_z orbital, ξ_p , giving a negligible contribution.

$$\lambda_I \simeq \frac{2(\varepsilon_p - \varepsilon_s)}{9V_{sp\sigma}^2} \xi_p^2 + \frac{9V_{pd\pi}^2}{2(\varepsilon_d - \varepsilon_p)^2} \xi_d \quad (2.53)$$

where $\varepsilon_{s,p,d}$ are the energies of s , p , d orbitals, respectively and $V_{sp\sigma}$ and $V_{pd\pi}$ are hopping parameters of the p orbital to the s and d orbital, respectively (Fig. 2.14).

This TB calculation gave the value of intrinsic SOC $\lambda_I = 12 \mu\text{eV}$ [55] and was confirmed by the first principle calculation [53]. These calculations also showed that

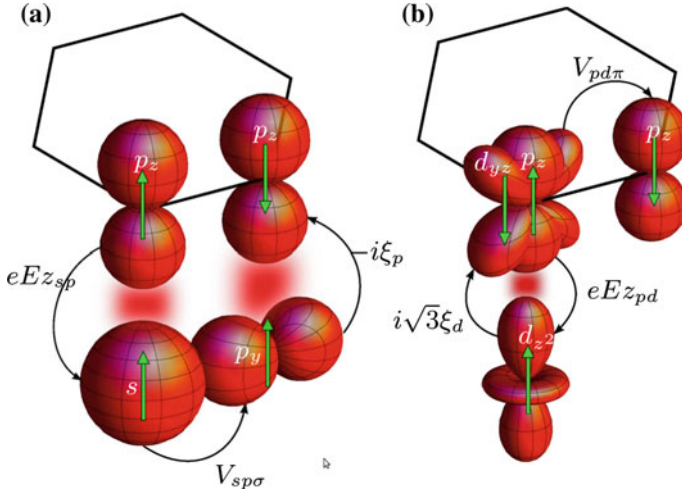


Fig. 2.15 A representative hopping path is responsible for Rashba SOC in Eq. (2.54) (Figure is taken from [55])

the Rashba term (zero in absence of electric field) is tunable with an external electric field E which is perpendicular to graphene plane (Fig. 2.15)

$$\lambda_R \simeq \frac{2eEz_{sp}}{3V_{sp\sigma}}\xi_p + \sqrt{3}\frac{eEz_{sp}}{(\varepsilon_d - \varepsilon_p)}\frac{3V_{pd\pi}}{(\varepsilon_d - \varepsilon_p)}\xi_d \quad (2.54)$$

where z_{sp} and z_{pd} are the expectation values $\langle s|\hat{z}|p_z\rangle$ and $\langle p_z|\hat{z}|d_{z^2}\rangle$, respectively, of the operator \hat{z} .

All these calculations predicted that the Rashba SOC is directly proportional to the electric field E , but the estimated values vary by about an order of magnitude from 5 μeV in Ref. [53] to 47 μeV in Ref. [50] and to 67 μeV in Ref. [57], for a typical electric field of $E = 1 \text{ V/nm}$. Furthermore, Ast and Gierz [60] used the TB model and directly considered the nearest-neighbor contribution from the electric field and obtained $\lambda_R = 37.4 \mu\text{eV}$.

In general, the intrinsic SOC of graphene is very weak, in the order of μeV and is unmeasurable. This makes some phenomena such as QSH effect unobservable in graphene, the material in which it was originally predicted [56]. A way to observe QSH effect in graphene is endowing it with heavy adatoms which increase SOC in graphene. This problem will be mentioned in Chap. 5.

2.4.2 Spin Transport in Graphene

The graphene SOC in the order of μeV as mentioned above should lead to spin relaxation times in the microsecond scale [9]. However, the experimental results is

in the order of nanoseconds, several orders of magnitude lower than the original theoretical prediction. In order to clarify the limitations and mechanisms for spin relaxation in graphene a lot of effort has been done by both experimentalists and theoreticians, but up to now this topic is still under debate. The first measurement of electron spin relaxation was performed by Tombros et al. [2] using the non-local spin valve measurement and Hanle spin precession method to study spin relaxation in mechanical exfoliated single-layer graphene (SLG) on SiO_2 substrate with mobility of the devices about $2,000 \text{ cm}^2 \text{ V}^{-1} \text{ s}^{-1}$. They extracted the spin relaxation time of few hundreds of ps and spin relaxation length of few μm at room temperature, similar to what one might expect for conventional metals or semiconductors. This value has been confirmed by several measurements [7, 61]. The spin transport was found to be relatively insensitive to the temperature and weakly dependent on the direction of spin injection and charge density. Due to the fast spin relaxation was attributed to the extrinsic SOC in the substrate and the way to grow graphene, spin measurements in many other kinds of graphene and substrates have been reported. The measurement of spin relaxation on epitaxially grown graphene on $SiC(0001)$ [62] is the first report of spin transport in graphene on a different substrate than SiO_2 . The value of spin relaxation τ_s was obtained in the order of few nanoseconds, one order of magnitude larger than in exfoliated graphene on SiO_2 . However the spin diffusion coefficient $D_s \approx 4 \text{ cm}^2/\text{s}$ is about 80 times smaller, yielding to 70 % lower value for spin relaxation length λ_s . The longer τ_s but much smaller D_s was later explained by the influence of localized states arising from the buffer layer at the interface between the graphene and the SiC surface that couple to the spin transport channel [63]. The measurement also reported that τ_s is weakly influenced by the temperature with reductions of D_s by more than 40 % and τ_s by about 20 % at room temperature. With the expectation that removing the underneath substrate helps to reduce the extrinsic SOC and leads to long spin relaxation time, the spin measurement on suspended graphene was performed [64]. Although a high mobility $\mu \approx 10^5 \text{ cm}^2 \text{ V}^{-1} \text{ s}^{-1}$, an increase up to an order of magnitude in spin diffusion coefficient ($D_s = 0.1 \text{ m}^2/\text{s}$) compared to SiO_2 supported graphene and long mean free path in the order of a μm were observed, indicating that much less scattering happens, the spin relaxation time remains a few hundreds of ps and spin relaxation length few μm . Other group used CVD method to grow graphene on copper (Cu) substrate and studied the effect of corrugation on spin relaxation time [65]. They observed the same spin relaxation time as in exfoliated graphene and showed that ripples in graphene flakes have minor effects on spin transport parameters.

The nature of spin relaxation is actually a fundamental debated issue. The DP [1, 66, 67] and the EY (EY) [68, 69] are two mechanisms usually discussed in the context of graphene. The EY mechanism is a suitable mechanism for spin relaxation in metals. In the EY mechanism, electron spin changes its direction during the scattering event thanks to the SOC which produces admixtures of spin and electron momentum in the wave functions. Due to these admixtures, scattering changes electron momentum and induces spin-flip probability at the same time and leads to a typical scaling behavior of spin relaxation time with momentum relaxation time $\tau_s^{EY} \sim \tau_p$. On the other hand, DP mechanism is an efficient mechanism for materials

with broken inversion symmetry. In these kinds of materials, SOC induces an effective momentum-dependent magnetic field about which electron spin precesses between scattering events. The longer time electron travels, the larger angle electron spin precesses and as a consequence, the more spin dephasing between electrons in the ensemble is accumulated. Therefore, spin relaxation time is inversely proportional to elastic scattering time $\tau_s^{DP} \sim \tau_p^{-1}$. W. Han and R.K. Kawakami performed systematic studies of spin relaxation in SLG and bilayer graphene (BLG) spin valves with tunneling contact [61]. They found that in SLG, the spin relaxation time varies linearly with momentum scattering time τ_p , indicating the dominance of EY spin relaxation whereas in BLG, τ_s and τ_p exhibit an inverse dependence, which indicates the dominance of DP mechanism. However, Pi et al. reported a surprising result that τ_s increases with decreasing τ_p in the surface chemical doping experiment with Au atoms on graphene [5], indicating that the DP mechanism is important there. This experiment led to the conclusion that charged impurity scattering is not the dominant mechanism for spin relaxation, despite its importance for momentum scattering. Even more puzzling, Zomer et al. [70] performed spin transport measurements on graphene deposited on boron nitride with mobilities up to $4 \cdot 10^4 \text{ cm}^2 \text{ V}^{-1} \text{ s}^{-1}$ and showed that neither EY nor DP mechanisms alone allow for a fully consistent description of spin relaxation. Furthermore, electron spin is expected to relax faster in BLG than in SLG because the SOC in BLG is one order of magnitude larger than the one in SLG due to the mixing of π and σ bands by interlayer hopping [71], but the experimental results showed an opposite behavior [61, 72]. The spin relaxation time in BLG has been reported in the order of few *nanoseconds* and show the dominance of DP spin scattering [61, 72]. Now we look at both mechanisms in more detail.

DP mechanism:

As one can see from Eq. (2.51), electron precesses about the effective magnetic field in plane $\mathbf{B}_{\parallel}(\mathbf{k}) \sim \mathbf{\Omega}(\mathbf{k})$ between scattering events. Random scattering induces motional narrowing of this spin precession causing spin relaxation (See Fig. 2.16). The spin relaxation rates for the α -th spin component following the DP mechanism are [9]

$$\frac{1}{\tau_{s,\alpha}^{DP}} = \tau^* \left(\langle \mathbf{\Omega}^2(\mathbf{k}) \rangle - \langle \mathbf{\Omega}_{\alpha}^2(\mathbf{k}) \rangle \right) \quad (2.55)$$

where τ^* is the correlation time of the random spin-orbit field. In graphene this value coincides with momentum relaxation time $\tau^* = \tau_p$ [9, 73] and the symbol $\langle \dots \rangle$ expresses an average over the Fermi surface. Because of $\langle \mathbf{\Omega}^2(\mathbf{k}) \rangle = (2\lambda_R/\hbar)^2$, $\langle \mathbf{\Omega}_z^2(\mathbf{k}) \rangle = 0$ and $\langle \mathbf{\Omega}_{x,y}^2(\mathbf{k}) \rangle = \frac{1}{2}(2\lambda_R/\hbar)^2$, the DP relation for spin relaxation in graphene is [1, 9]

$$\tau_{s,z}^{DP} = \frac{\hbar^2}{4\lambda_R^2\tau_p}, \quad \text{and} \quad \tau_{s,\{x,y\}}^{DP} = 2\tau_{s,z}^{DP} = \frac{\hbar^2}{2\lambda_R^2\tau_p} \quad (2.56)$$

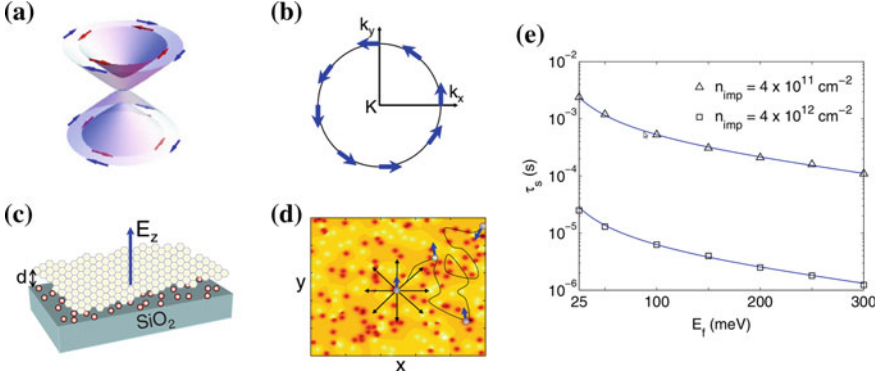


Fig. 2.16 DP spin relaxation in graphene: **a** Dirac coin when SOC is included. **b** $B_{\parallel}(\mathbf{k})$ along the Fermi circle. **c** Charged impurities in substrate induce electric field in graphene. **d** Illustration of the spin relaxation in a spatially random potential due to the charged carriers. **e** Calculated spin relaxation time τ_s as a function of the Fermi energy E_f (Figure is taken from [9])

Because the spin relaxation time is inversely proportional to the momentum relaxation time, the DP spin relaxation length is independent of mean free path [1].

$$\lambda_s = \sqrt{D\tau_s} = \sqrt{\frac{1}{2}v_F^2\tau_p\tau_s} = \frac{\hbar v_F}{2\sqrt{2}\lambda_R} \quad (2.57)$$

The analytical estimates and Monte Carlo simulations [9] with DP mechanism show that the corresponding spin relaxation times are between micro- to milliseconds (See Fig. 2.16) several orders of magnitude larger than the experimental results.

EY mechanism:

As mentioned above, intrinsic SOC obtained by TB model and density functional calculation is in the order of tens μeV [50, 55, 57, 58], much smaller and can be neglected in comparison to the Rashba SOC. In the case of slowly varied Rashba SOC induced by electric field or ripples, the Hamiltonian can be written in form

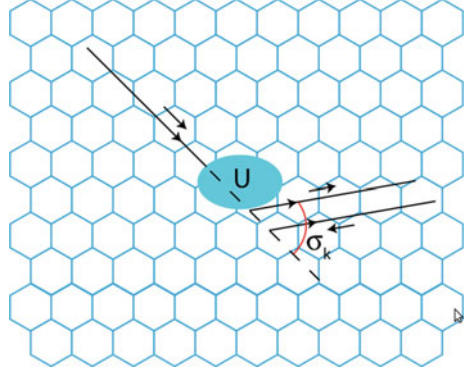
$$\mathcal{H} = -i\hbar v_F \boldsymbol{\sigma} \cdot \nabla + \lambda_R (\boldsymbol{\sigma} \times \mathbf{s}) \quad (2.58)$$

Because of the Rashba SOC, Bloch states with well-defined spin polarization are no longer eigenstates of the Hamiltonian. The Bloch eigenstates of above Hamiltonian are [69]

$$\Psi_{\mathbf{k},\pm} = \left[\left(\frac{1}{\frac{\epsilon_{\mathbf{k}\pm}}{\hbar v_F k}} e^{i\theta_{\mathbf{k}}} \right) \otimes |\uparrow\rangle \pm i \left(\frac{\epsilon_{\mathbf{k}\pm}}{\hbar v_F k} e^{i\theta_{\mathbf{k}}} \right) \otimes |\downarrow\rangle \right] e^{i\mathbf{k}\cdot\mathbf{r}}. \quad (2.59)$$

where $\theta_{\mathbf{k}} = \arctan(k_y/k_x)$ and the energy $\epsilon_{\mathbf{k}\pm} = \pm\lambda_R + \sqrt{(\hbar v_F k)^2 + \lambda_R^2}$ is obtained from Eq. (2.49) with $\lambda_I = 0$. When $\lambda_R = 0$, eigenstates in Eq. (2.59)

Fig. 2.17 Sketch of scattering by a potential $U(\mathbf{r})$ in the chiral channels (Figure is taken from [69])



have their spin pointing along (helicity +) or opposite to (helicity -) the direction of motion. This is not true when $\lambda_R \neq 0$ but in the case of $\lambda_R/\epsilon_F \ll 1$, using perturbation theory we can identify each of these eigenstates with chiral states \pm [69]. Let's consider the Born approximation of the scattering problem of electron in the graphene under the local scattering potential $U(\mathbf{r})$ which is diagonal in the sublattice and spin degrees of freedom. The scattering amplitudes $f_{\pm}^0(\theta)$ for chiral channels \pm of an incoming electron with positive chirality in the case of $\lambda_R = 0$ are (For detail derivation, see Ref. [69])

$$\begin{aligned} f_+^0(\theta) &= -(\hbar v_F)^{-1} \sqrt{\frac{k}{8\pi}} U_{\mathbf{q}} e^{-i\theta} (1 + \cos\theta) \\ f_-^0(\theta) &= -(\hbar v_F)^{-1} \sqrt{\frac{k}{8\pi}} U_{\mathbf{q}} i e^{-i\theta} \sin\theta \end{aligned} \quad (2.60)$$

where $U_{\mathbf{q}}$ is the Fourier transformation of the scattering potential evaluated at the transferred momentum $\mathbf{q} = \mathbf{k}' - \mathbf{k}$ and angle θ (see Fig. 2.17) between the outgoing momentum \mathbf{k}' and incoming momentum \mathbf{k} .

When Rashba SOC is turned on these amplitudes become

$$\begin{aligned} f_+^{\lambda_R}(\theta) &= -(\hbar v_F)^{-2} \sqrt{\frac{1}{8\pi k_+}} (\epsilon + (\epsilon - 2\lambda_R)\cos\theta) U_{\mathbf{q}_+} e^{-i\theta} \\ f_-^{\lambda_R}(\theta) &= -(\hbar v_F)^{-2} \sqrt{\frac{1}{8\pi k_-}} (\epsilon + 2\lambda_R) U_{\mathbf{q}_-} i e^{-i\theta} \sin\theta \end{aligned} \quad (2.61)$$

where $k_{\pm} = (\hbar v_F)^{-1} \sqrt{\epsilon^2 \mp 2\epsilon\lambda_R}$ and $\mathbf{q}_{\pm} = \mathbf{k}'_{\pm} - \mathbf{k}$.

Let us define the probability for a spin-flip process from the changes in the scattering in both chiral channels due to the presence of the SOC.

$$S(\theta) = \frac{\sum_{\pm 1} |f_{\pm}^0(\theta)| |f_{\pm}^{\lambda_R}(\theta) - f_{\pm}^0(\theta)|}{\sum_{\pm 1} |f_{\pm}^0(\theta)|^2} \quad (2.62)$$

This is the amount of spin relaxed in the direction defined by θ . The total amount of spin relaxation during a scattering event can be defined as the average of this quantity over the Fermi surface:

$$S = \langle S(\theta) \rangle = \frac{1}{2\pi} \int d\theta S(\theta, \epsilon = \epsilon_F) \quad (2.63)$$

It is easy to see that $f_{\pm}^{\lambda_R}(\theta) - f_{\pm}^0(\theta) \sim \lambda_R/\epsilon_F$ from expanding of Eq. (2.61) in powers of λ_R/ϵ_F . This implies that $S(\theta) \sim \lambda_R/\epsilon_F$ which is independent with the scattering potentials $U(\mathbf{r})$. This result was obtained in Ref. [1] for the case of weak scatterers, and later in Ref. [69] for the cases of scattering by boundary, strong scatterers and clusters of impurities which can not be treated in perturbation theory. Assuming this behavior, the EY relation for graphene can be easily found. Indeed, the change of spin orientation at each collision is $S \sim \lambda_R/\epsilon_F$. The total change of spin orientation after N_{col} collisions is of the order of $\sqrt{N_{col}}\epsilon_F/\lambda_R$. Dephasing occurs when $\sqrt{N_{col}}\epsilon_F/\lambda_R \sim 1$ and of course, after a time $\tau_s^{EY} = N_{col}\tau_p$. Hence we obtain the EY relation

$$\tau_s^{EY} \approx \frac{\epsilon_F^2}{\lambda_R^2} \tau_p \quad (2.64)$$

This is the EY relation for graphene. It is worth to mention that the spin relaxation time τ_s here not only is proportional to momentum relaxation time τ_p but also depends on the carrier density through Fermi energy ϵ_F . The spin relaxation length in EY mechanism is proportional to mean free path ℓ_e

$$\lambda_s = \sqrt{D\tau_s} = \sqrt{\frac{1}{2}v_F^2\tau_p\tau_s} \sim \ell_e \frac{\epsilon_F}{\sqrt{2}\lambda_R} \quad (2.65)$$

Despite the fact that some experiments have reported that $\tau_s \sim \tau_p$, indicating the dominance of EY mechanism in spin relaxation in graphene, the discrepancy between theoretical calculations and experimental data is still large. Furthermore, the derivations of both EY and DP for graphene are based on the strong coupling of momentum and pseudospin which is unsuitable close to the Dirac point. In Chap. 5, we propose a new mechanism which is the heart of this PhD thesis to explains the fast spin relaxation in graphene by the entanglement of spin and pseudospin degrees of freedom.

References

1. D. Huertas-Hernando, F. Guinea, A. Brataas, Phys. Rev. Lett. **103**, 146801 (2009)
2. N. Tombros et al., Nature (London) **448**, 571 (2007)
3. N. Tombros et al., Phys. Rev. Lett. **101**, 046601 (2008)
4. C. Jozsa et al., Phys. Rev. Lett. **100**, 236603 (2008)
5. K. Pi et al., Phys. Rev. Lett. **104**, 187201 (2010)

6. T. Maassen et al., Phys. Rev. B **83**, 115410 (2011)
7. W. Han et al., Phys. Rev. Lett. **105**, 167202 (2010)
8. A.H. Castro Neto, F. Guinea, N.M.R. Peres, K.S. Novoselov, A.K. Geim, Rev. Mod. Phys. **81**, 109 (2009)
9. C. Ertler et al., Phys. Rev. B **80**, 041405 (2009)
10. E.F. Luis, F. Torres, S. Roche, J.C. Charlier, *Introduction to Graphene-Based Nanomaterials From Electronic Structure to Quantum Transport* (Cambridge, 2013)
11. S.D. Sarma, S. Adam, E.H. Hwang, E. Rossi, Rev. Mod. Phys. **83**, 407 (2011)
12. M.O. Goerbig, Rev. Mod. Phys. **83**, 1193 (2011)
13. E. McCann, K. Kechedzhi, V.I. Falko, H. Suzuura, T. Ando, B.L. Altshuler, Phys. Rev. Lett. **97**, 146805 (2006)
14. F.V. Tikhonenko, D.W. Horsell, R.V. Gorbachev, A.K. Savchenko, Phys. Rev. Lett. **100**, 056802 (2008)
15. M.I. Katsnelson, K.S. Novoselov, A.K. Geim, Nat. Phys. **2**, 620 (2006)
16. K.S. Novoselov, A.K. Geim, S.V. Morozov, D. Jiang, Y. Zhang, S.V. Dubonos, I.V. Grigorieva, A.A. Firsov, Science **306**, 666 (2004)
17. K.S. Novoselov, A.K. Geim, S.V. Morozov, D. Jiang, M.I. Katsnelson, I.V. Grigorieva, S.V. Dubonos, A.A. Firsov, Nature (London) **438**, 197 (2005)
18. A.K. Geim, K.S. Novoselov, Nat. Mater. **6**, 183 (2007)
19. N.H. Shon, T. Ando, J. Phys. Soc. Jpn. **67**, 2421 (1998)
20. S. Roche, N. Leconte, F. Ortmann, A. Lherbier, David Soriano, Jean-Christophe Charlier, Solid State Commun. **152**, 1404–1410 (2012)
21. A. Lherbier, B. Biel, Y.M. Niquet, S. Roche, Phys. Rev. Lett. **100**, 036803 (2008)
22. P.A. Lee, T.V. Ramakrishnan, Rev. Mod. Phys. **57**, 2 (1985)
23. Y.Y. Zhang, J. Hu, B.A. Bernevig, X.R. Wan, X.C. Xie, W.M. Liu, Phys. Rev. Lett. **102**, 106401 (2009)
24. F. Karlicky, R. Zboil, M. Otyepka, J. Chem. Phys. **137**, 034709 (2012)
25. F. Evers, A.D. Mirlin, Rev. Mod. Phys. **80**, 1355 (2008)
26. J.O. Sofo, A.S. Chaudhari, G.D. Barber, Phys. Rev. B **75**, 153401 (2007)
27. E.H. Lieb, Phys. Rev. Lett. **62**, 1201 (1989)
28. V.O. Yazyev, Phys. Rev. Lett. **101**, 037203 (2008)
29. D. Soriano, N. Leconte, P. Ordejon, J.C. Charlier, Juan J. Palacios, Stephan Roche, Phys. Rev. Lett. **107**, 016602 (2011)
30. N. Leconte, D. Soriano, S. Roche, P. Ordejon, Jean C. Charlier, Juan J. Palacios, ACS Nano **5**, 3987–3992 (2011)
31. J. Zhou et al., Nano Lett. **9**, 3867–3870 (2009)
32. A.W. Robertson et al., Nat. Commun. **3**, 1144 (2012)
33. A. Lherbier, S.M.M. Dubois, X. Declerck, S. Roche, Y.M. Niquet, J.C. Charlier, Phys. Rev. Lett. **106**, 046803 (2011)
34. A. Lherbier, S.M.M. Dubois, X. Declerck, Y.M. Niquet, S. Roche, J.C. Charlier, Phys. Rev. B **86**, 075402 (2012)
35. F. Banhart, J. Kotakoski, A.V. Krashennnikov, ACS Nano **5**, 26–41 (2011)
36. J. Kotakoski, A.V. Krashennnikov, U. Kaiser, J.C. Meyer, Phys. Rev. Lett. **106**, 105505 (2011)
37. V. Kapko, D.A. Drabold, M.F. Thorpe, Phys. Stat. Solidi B **247**, 1197–1200 (2010)
38. Y. Li, F. Inam, F. Kumar, M.F. Thorpe, D.A. Drabold, Phys. Stat. Solidi B **248**, 2082–2086 (2011)
39. E. Holmström et al., Phys. Rev. B **84**, 205414 (2011)
40. A. Lherbier, S. Roche, O.A. Restrepo, Y.-M. Niquet, A. Delcorte, J.-C. Charlier, Nano Res. **6**, 326–334 (2013)
41. O.V. Yazyev, S.G. Louie, Nat. Mater. **9**, 806 (2010)
42. D. Gunlycke, C.T. White, Phys. Rev. Lett. **106**, 136806 (2011)
43. A.W. Tsien et al., Science **336**, 1143–1146 (2012)
44. P.Y. Huang, C.S. Ruiz-Vargas, A.M. van der Zande, W.S. Whitney, M.P. Levendorf, J.W. Kevek, S. Garg, J.S. Alden, C.J. Hustedt, Y. Zhu, J. Park, P.L. McEuen, D.A. Muller, Nature **469**, 389 (2011)

45. Q. Yu et al., *Nat. Mater.* **10**, 443–449 (2011)
46. K.W. Clark et al., *ACS Nano* **7**, 7956–7966 (2013)
47. D.W. Boukhvalov, M.I. Katsnelson, *Nano Lett.* **8**, 4373–4379 (2008)
48. P. Nemes-Incze et al., *Appl. Phys. Lett.* **94**, 023104 (2011)
49. D.L. Duong et al., *Nature* **490**, 235–239 (2012)
50. D. Huertas-Hernando, F. Guinea, A. Brataas, *Phys. Rev. B* **74**, 155426 (2006)
51. L.H. Thomas, *Nature* **117**, 514 (1926)
52. Z. Qiao, H. Jiang, X. Li, Y. Yao, Q. Niu, *Phys. Rev. B* **85**, 115439 (2012)
53. M. Gmitra, S. Konschuh, C. Ertler, C. Ambrosch-Draxl, J. Fabian, *Phys. Rev. B* **80**, 235431 (2009)
54. I. Emmanuel Rashba, *Phys. Rev. B* **79**, 161409(R) (2009)
55. S. Konschuh, M. Gmitra, J. Fabian, *Phys. Rev. B* **82**, 245412 (2010)
56. C.L. Kane, E.J. Mele, *Phys. Rev. Lett.* **95**, 226801 (2005)
57. H. Min et al., *Phys. Rev. B* **74**, 165310 (2006)
58. Y. Yao et al., *Phys. Rev. B* **75**, 041401(R) (2007)
59. J.C. Boettger, S.B. Trickey, *Phys. Rev. B* **75**, 121402(R) (2007)
60. C.R. Ast, I. Gierz, *Phys. Rev. B* **86**, 085105 (2012)
61. W. Han, R.K. Kawakami, *Phys. Rev. Lett.* **107**, 047207 (2011)
62. T. Maassen et al., *Nano Lett.* **12**, 1498–1502 (2012)
63. T. Maassen, J.J. van den Berg, E.H. Huisman, H. Dijkstra, F. Fromm, T. Seyller, B.J. van Wees, *Phys. Rev. Lett.* **110**, 067209 (2013)
64. M.H.D. Guimaraes, A. Veligura, P.J. Zomer, T. Maassen, I.J. Vera-Marun, N. Tombros, B.J. van Wees, *Nano Lett.* **12**, 3512–3517 (2012)
65. A. Avsar et al., *Nano Lett.* **11**, 2363–2368 (2011)
66. M.I. D'yakonov, V.I. Perel, *Zh. Eksp. Teor. Fiz.* **60**, 1954 (1971)
67. M.I. D'yakonov, V.I. Perel, *Sov. Phys. Solid State* **13**, 3023 (1971)
68. R.J. Elliot, *Phys. Rev.* **96**, 266 (1954)
69. H. Ochoa, A.H. Castro, Neto, F. Guinea, *Phys. Rev. Lett.* **108**, 206808 (2012)
70. P.J. Zomer, M.H.D. Guimaraes, N. Tombros, B.J. van Wees, *Phys. Rev. B* **86**, 161416(R) (2012)
71. F. Guinea, *New J. Phys.* **12**, 083063 (2010)
72. T.Y. Yang et al., *Phys. Rev. Lett.* **107**, 047206 (2011)
73. J. Fabian, A. Matos-Abiague, C. Ertler, P. Stano, I. Zutic, *Acta Phys. Slov.* **57**, 565 (2007)



<http://www.springer.com/978-3-319-25569-9>

Charge and Spin Transport in Disordered
Graphene-Based Materials

Van Tuan, D.

2016, XVI, 153 p., Hardcover

ISBN: 978-3-319-25569-9